Dynamic recrystallization behavior of low carbon steel during the flexible rolling process: Modeling and characterization

Caiyi Liu[1], Carlo Mapelli[2], Yan Peng[1,*], Silvia Barella[2], Shicheng Liang[1], Andrea Gruttadauria[2], Marco Belfi[2]

1. National Engineering Research Center for Equipment and Technology of Cold Rolled Strip, Yanshan University, Qinhuangdao 066004, China

2. Department of Mechanical Engineering, Politecnico di Milano, Milan, 20156, Italy

* Correspondence: pengyan@ysu.edu.cn

Abstract: Dynamic recrystallization (DRX) is the predominant softening mechanism under high-temperature large-plastic deformation and determines the microstructure evolution of carbon steel. In the present study, we propose an equivalent substitution method to investigate the coupling effect of deformation conditions in the thickness transition zone on microstructural evolution during the flexible rolling process. Low carbon steel was compressed using a Gleeble 3800-GTC thermal-mechanical physical simulation system at temperatures ranging from 900 to 1100 ℃ and strain rates ranging from 0.01 s^{-1} to 10 s^{-1}. The flow stress behaviors under different deformation conditions were discussed, and the results were subsequently used to determine the critical value for the occurrence of DRX. The results show that there is a linear relationship between critical strain and peak strain. Accordingly, the relationship between strain rate and temperature was established using the Zener-Hollomon equation. Further, a new DRX model was proposed by combining the theoretical implications of previous models. The effectiveness of the experimental model and predicted model was statistically evaluated to accurately determine the DRX volume fraction of the experimental steel. Based on the dynamic material model, a hot processing map of the experimental steel was also developed to evaluate the steel's hot workability. Instability regions were mainly observed under high strain rates and temperatures. Finally, the microstructure of the experimental steel was analyzed under specific deformation parameters. The results demonstrated that DRX behavior decreased as the upper roller was raised and the lower roller was lowered during the flexible rolling process.

Keywords: Flexible rolling; Dynamic recrystallization; Thermal compression; Processing map; Microstructure evolution

1 Introduction

Removing the old roll set from the mill stand and inserting a new roll set into the mill stand is referred as roll change (RC). The rolling process is forced to stop during the RC process, which poses a great challenge for researching seeking to increase the final yield and continuously produce rolled strips. In the present paper, flexible rolling technology (Fig. 1) is proposed to solve the problem of the downtime caused by RC. In this study, red and green represent the old rolls and new rolls, respectively. When the roll becomes worn, the flexible rolling process leads to inline work roll changes. The upper roller is then raised and the lower roller lowered, starting with a temporary increase in strip thickness, i.e., the shape of the rolled strip changes along the rolling direction, as shown in Fig. 1. During the flexible rolling process, work hardening (WH) and dynamic softening are two important factors that determine the microstructure and mechanical properties of the hot rolled strip [1-5]. Dynamic softening also plays a vital role in refining the grain and loading distribution when optimizing the rolling process [6-8].

In recent years, dynamic softening has been explored in several experimental and theoretical studies. The DRX kinetics model was established by Sellars et al. [9]. In a follow up study, Yada et al. [10], Kim et al. [11, 12], and Kopp et al. [13] modified the DRX kinetics model based on different deformation parameters. Jonas [14] and Serajzadeh [15] made great efforts to build a DRX kinetics models suitable for different kinds of steel, which is widely accepted as the classical model for calculating the volume fraction of DRX. However, the above models still have some

limitations, and many of their fitting parameters do not have obvious physical meanings. More recently, because the DRX model is based on the evolution of the Johnson-Mehl-Avrami-Kolonagorov static recrystallization model, Liu et al. [16] proposed another DRX model to represent the 'slow-rapid-slow' property of DRX development. However, the constant in the model is not directly related to the strain rate and deformation temperature; furthermore, the model's accuracy between experimental and predicted X_{drx} values has not been investigated. Considering the limitations of the theory in [16]. Li et al. [17] proposed a theory that the constant in the new DRX model is related to the temperature based strain rate compensation factor Z. The prediction performance and reliability of the models were further scientifically evaluated.

There are many extensive studies on using microstructure characterization under different deformation conditions to illustrate the interactions between microstructure evolution and DRX behaviors. Ji et al. [18] studied the DRX behavior and microstructure evolution of 33Cr23Ni8Mn3N steel under a temperature range of 1000-1180 ℃ and a strain rate of 0.01-10 s^{-1}. The results showed that the DRX grain size increases by increasing the temperature and decreasing the strain rate. Shen et al. [19] investigated an extruded Al-Cu-Li alloy via compression tests at various temperatures and strain rates and used the EBSD system to analyze the microstructure evolution of the extruded Al-Cu-Li alloy. Based on the evolution of the grain boundary, the DRX was controlled by grain boundary bulging and grain boundary transformation. Zhang et al. [20] observed the microstructure evolution of an Al-Mg-Si aluminum alloy through EBSD analysis. The results showed that the type of DRX was associated with the deformation temperature. Zhao et al.[21] constructed a 3D instability map and 3D power dissipation map to evaluate the hot workability of a high strength low alloy steel. The results showed that the flow instability and DRX degree were closely related to the power dissipation efficiency. When the power dissipation efficiency was below 25%, the DRX process developed inadequately, leading to a high risk of flow instability. Because the deformation temperature, strain, and strain rate both affect the microstructure evolution of the material, several studies have focused on how the deformation temperature and strain rate affect DRX behavior [22-24], and the DRX model was established based on the above factor [25-27]. However, few studies have investigated the deformation state, mainly focusing on whether the strain reaches the critical strain of DRX. Although extensive research has been carried out on hot processing mapping, model correction, stress-strain curve correction, and meta dynamics, no single study adequately covers the relationships between the deformation parameters, power dissipation efficiency, microstructure, and DRX mechanism for the purposes of investigating DRX behavior during the flexible rolling process. Therefore, the need remains for a comprehensive and systematic analysis of DRX behavior through thermal compression experiments.

In summary, the deformation temperature, strain rate, and deformation state during the flexible rolling process are interactively coupled to affect DRX behavior. The thickness transient zone along the rolling direction has the most significant impact on the DRX behavior of the rolled strip. In the present study, the equivalent substitution method was used to identify the relationship between DRX, hot processing, and microstructure evolution during the flexible rolling process. The DRX behavior of low carbon steel was studied in detail according to an isothermal compression test under different deformation conditions. The investigation included flow stress analysis, DRX analysis, and hot processing map analysis. This study will improve the understanding of DRX behaviors during the flexible rolling process and provide a method to optimize the relevant processing parameters.

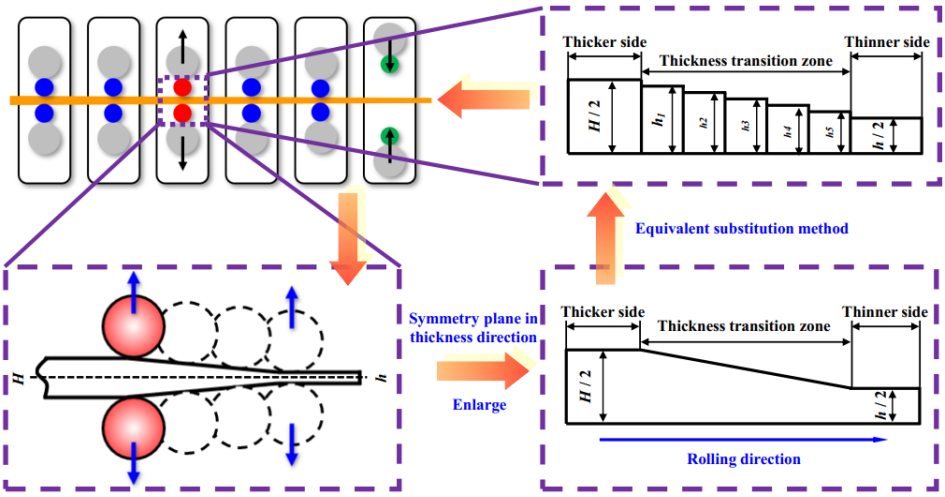

Fig. 1. The flexible rolling process and research methodology used in this paper

2. Materials and methods

2.1. Experimental materials

A hot rolled low carbon strip was used in this experiment; the chemical composition of the strip is shown in Table 1. The element content was measured using a sulfur / carbon analyzer and X-Ray fluorescence (XRF). The Ac1 and Ac3 temperatures were determined from the dilatometric data obtained by the dilatometer DIL 402. As shown in Fig. 2. The A_{C1} and A_{C3} of the strip were determined to be 706 and 828 °C, respectively. The experimental temperature was determined based on the obtained critical transition temperature. The original microstructure of the tested steel is shown in Fig. 3. It can be seen from the figure that the original microstructure consisted of austenite equiaxed grains The average grain size was measured to be about 68±5 μm by using the intercept method.

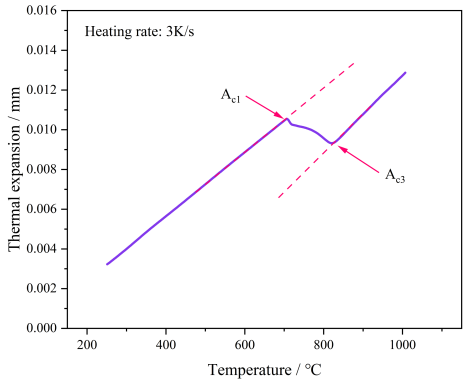

Fig. 2. Variation in thermal expansion with temperature during the heating process of the experimental steel.

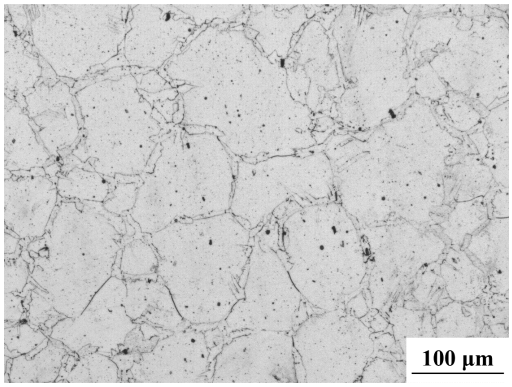

Fig. 3. Microstructure of the studied steel before hot deformation.

2.2. Experimental details

To investigate the effect of DRX on the macroscopic flow behavior during high-temperature deformation, the equivalent substitution method was used to physically simulate the flexible rolling process, i.e., when the upper roller is raised and the lower roller is lowered, the deformation state of the rolled strip in the rolling direction is different. This paper simulates the different deformation states using a single pass compression test of small bars on a Gleeble 3800-GTC thermal-mechanical physical simulation system. The specimen cut from the strip was 10 mm in diameter and 15 mm in height. In this work, the deformation temperature of the experimental steel was higher than austenitization temperature to ensure that all the experiments would yield complete austenitization during the hot deformation process. The specific experimental procedure and deformation parameters are shown in Fig. 4. Before the experiment, the cylindrical sample was coated on both sides with a molybdenum disulfide lubricant. A tantalum foil with a thickness of 0.1 mm was placed between the cylindrical sample and the chuck to reduce friction, avoid adhesion, and improve stability and uniformity during the deformation process. The graphite was cut into a disc with a diameter 2 mm larger than the initial diameter of the specimen and inserted between the indenter and the specimen to increase the resistance at the interface and ensure a uniform temperature in the axial direction of the sample. A K-type thermocouple was placed on the longitudinal center of the sample to measure the temperature. Prior to hot compression, all specimens were heated to 1200 ℃ at a heating rate of 10 ℃/s and soaked for 180 s to obtain a uniform microstructure. Then, the specimens were cooled to a deformation temperature at a rate of 5 ℃/s and held for 30 s to eliminate the temperature gradient. Subsequently, the specimens were subjected to unidirectional hot compression experiments in an argon atmosphere with a reduction of 10-60% to investigate the DRX behavior under different deformation conditions. The deformation temperature range was set to 900-1100 °C (with an interval of 50 °C) and strain rates of 0.01, 0.1, 1, and 10 s^{-1}. To retain the austenite DRX microstructure under a high temperature, the deformed samples were rapidly quenched to room temperature, and the deformed samples were cut parallel to the center of the compression axis to observe the microstructure of the central area. The sample was etched with Bechet-Beaujard (water based saturated picric acid, 80 ℃, a few drops of hydrochloric acid and shampoo) for 10-15 s after being polished. Subsequently, the microstructure was observed using a Nikon Eclipse LV150N optical microscope (OM).

Table 1 Chemical composition of the experimental steel (wt.%).

C	Si	Gr	Mn	P	S	Cu	Al	Fe
0.121	0.063	0.007	0.104	0.023	0.256	0.039	0.097	bal.

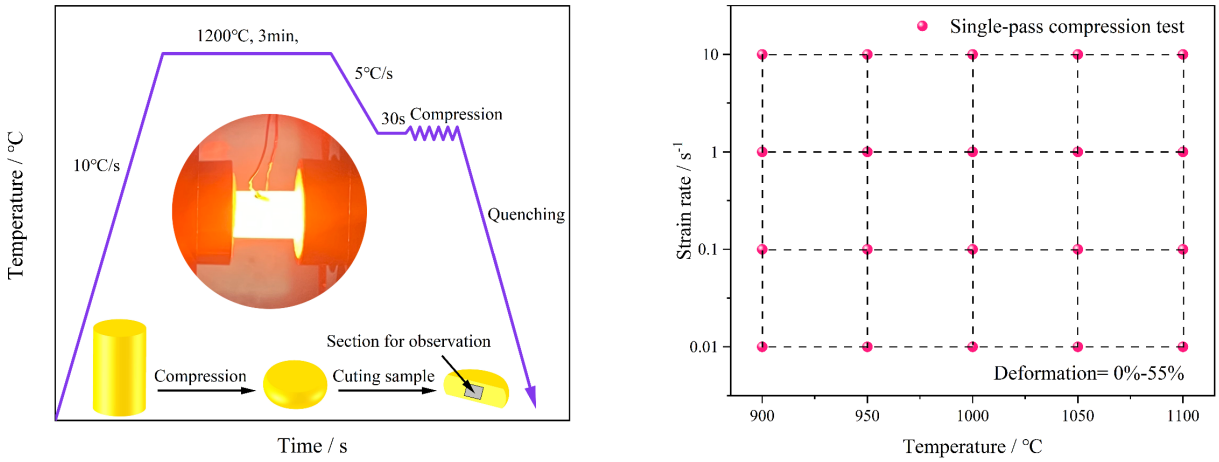

Fig. 4. Experimental design: (a) experimental procedure and (b) deformation parameters.

3. Results and discussion

3.1. Flow stress behavior

The true stress-strain curves of the test steel under different deformation conditions are shown in Fig. 5. This figure illustrates the significant effects of temperature and strain rate on the flow stress. All the true stress-strain curves

exhibit peak stress, which is consistent with recent studies [28]. Here, the peak stress decreases with an increase in temperature at a constant strain rate and increases with an increase in strain rate. For example, when the strain rate is 0.01 s^{-1}, the peak stress decreases from 84.6 MPa at 900 ℃ to 37.89 MPa at 1100 ℃. When the deformation temperature is 900 ℃, the peak stress increases from 84.6 MPa at 0.01 s^{-1} to 220.5 MPa at 10 s^{-1}. The steady-state flow stress reflects the dynamic equilibrium between WH and dynamic softening i.e., the two phenomena of WH and dynamic softening were present during the high-temperature deformation of the experimental steel. More broadly, two softening mechanisms exist in the dynamic softening process: dynamic recrystallization (DRX) and dynamic recovery (DRV). Previously published studies have shown that DRX and DRV can be distinguished from variation in the flow stress curve [29-33]. The two dynamic softening processes are independently reconstructed in Fig. 6 to illustrate the different softening mechanisms. The softening process caused by DRV occurs in all four regions, while DRX is initiated at the critical strain ε_c^{DRX}. When the strain is lower than the critical strain, the energy generated by the deformation is not enough to achieve the driving force needed to produce DRX. WH and DRV are the two dominant processes, though the softening mechanism is mainly DRV. The DRV curve shows that the flow stress will reach a steady state without any peak, with an increase in strain. Notably, the critical strain for DRV is always lower than that for DRX [34]. With an increase in the deformation state during high-temperature deformation, the WH rate gradually decreases, and DRX occurs once the strain exceeds the critical value. The occurrence of DRX makes the curve flatten. Then, the flow stress gradually reaches the peak and decreases, which indicates that various degrees of softening have occurred during the deformation process. The DRX curve can be divided into the following stages: I (region C). When the strain exceeds a critical value, DRX begins with the driving force of removing dislocations, resulting in a slow increase in flow stress up to a maximum value; during this process, the softening effect caused by DRX and DRV becomes more evident [35]. Then, the dynamic softening mechanism prevails over the work hardening that occurs afterwards. II (region D). Region D represents the complete DRX stage, and the flow stress reaches a steady state due to the combined effects of DRV and DRX.

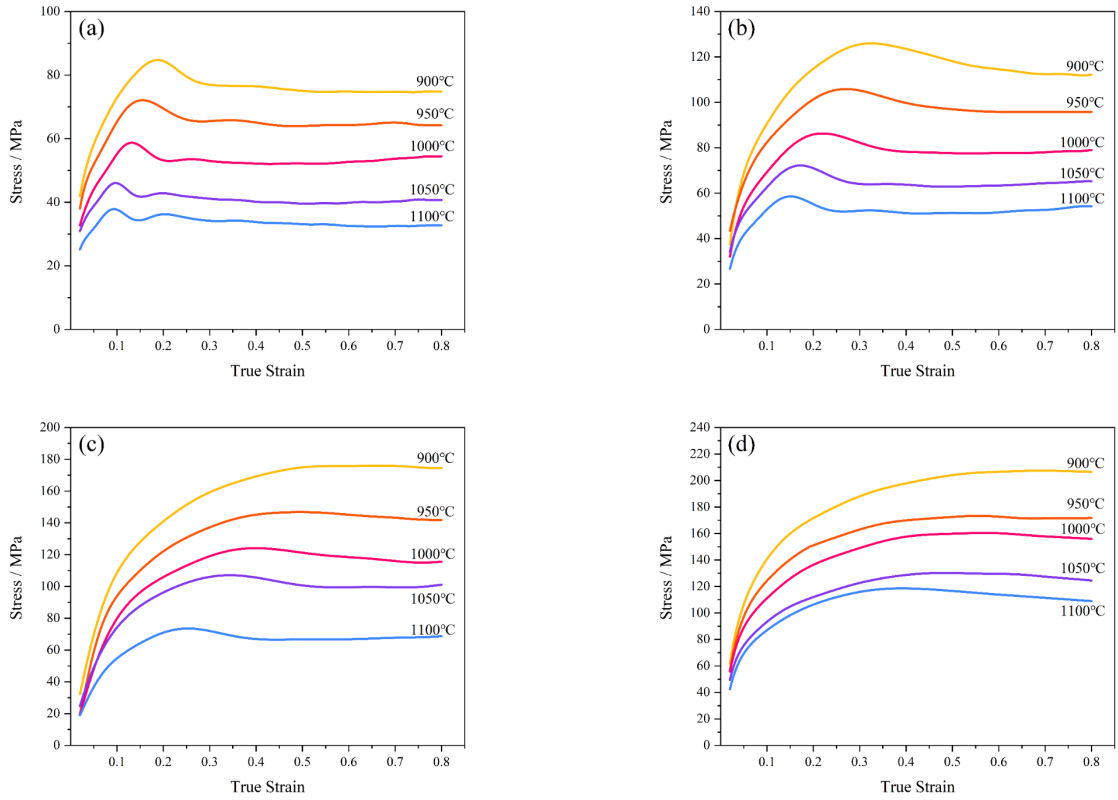

Fig. 5. Flow stress curves at different strain rates: (a) 0.01 s^{-1}, (b) 0.1 s^{-1}, (c) 1 s^{-1}, and (d) 10 s^{-1}.

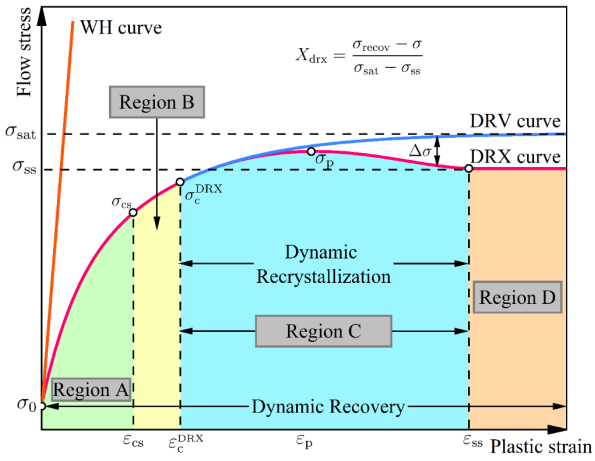

Fig. 6. Schematic representations of the flow stress curves.

Critical strain is a crucial parameter for DRX and mainly depends on the accumulated energy of the deformation process. Generally, there are two methods to obtain the DRX critical strain. One involves determining the microscopic grain structure of the quenched sample via metallographic observation, while the other involves determining the flow stress through mathematical modeling. Compared with the mathematical modeling method, metallographic observations can be difficult to infer due to phase transformations in the quenching process. Moreover, the preparation of multiple samples is required for quenching experiments to determine the critical strain ε_c. Therefore, the metallographic observation method is not a simple, fast, or objective means to estimate the critical strain.

In recent years, the mathematical modeling method has been widely used to describe special points of flow stress curves and determine the critical strain of DRX [36-38]. In this work, the derivative of the work hardening rate $|-d\theta/d\sigma|$ versus σ was calculated, and the minimum value was taken as the inflection point of the work hardening rate $|d\sigma/d\varepsilon|$ versus the σ curve. The critical stress of DRX is directly shown in the curves of Fig. 7. This method was proven by Mirzadeh and Najafizadeh [39] and Poliak and Jonas [40].

In Fig. 7, σ_p is the peak stress, σ_{ss} is the stable stress, σ_{sat} is the saturation stress, and σ_c is the critical stress. Here, σ and σ_{ss} can be obtained from the flow stress curves. The saturated stress σ_{sat} is the intercept of the work hardening rate and the inflection point σ_c tangent of the stress on the x axis. Hence, the corresponding critical strain to initiation can be obtained from the flow stress curve. Fig. 8 shows the work hardening rate curves under different deformation temperatures along with the strain rates. During the initial stage, the main mechanism is WH and DRV, resulting in the work hardening rate decreasing rapidly with an increase in stress. This phenomenon is due to the high generation rate of dislocations during the initial work hardening period. The softening effect induced by DRV occurs rapidly. As the stress increases further, the rate of decrease in WH slows. This period was proposed to be related to the formation process of subgrain structures [41]. When the deformation state exceeds the critical stress, the WH, DRV, and DRX are the three dominant mechanisms informing the progression of high temperature deformation. The work hardening rate decreases faster with an increase in stress and reaches zero at maximum peak stress (i.e., $\sigma = \sigma_p$). Afterward, the flow stress decreases with an increase in deformation until WH becomes zero again, corresponding to the steady stress σ_{ss}. The results confirm (Fig. 8) that the critical stress decreases with increases in temperature at a constant strain rate. Fig. 9 illustrates the relationship between σ_p and σ_c, ε_p, and ε_c under different deformation conditions, indicating that the relations follow a linear equation, which can be obtained by linear fitting. i.e., $\varepsilon_c/\varepsilon_p = 0.562$, $\sigma_c/\sigma_p = 0.964$.

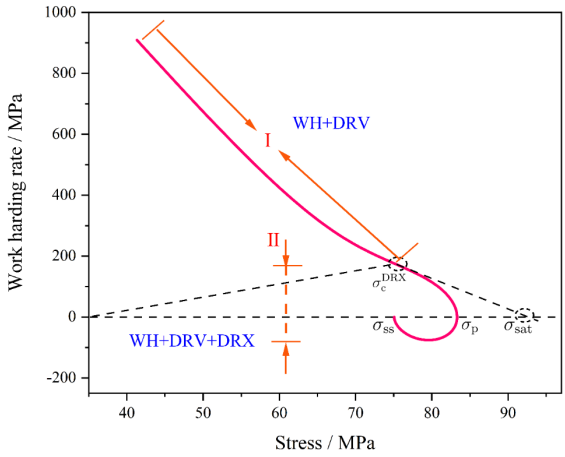

Fig. 7. Work hardening rate and stress curve.

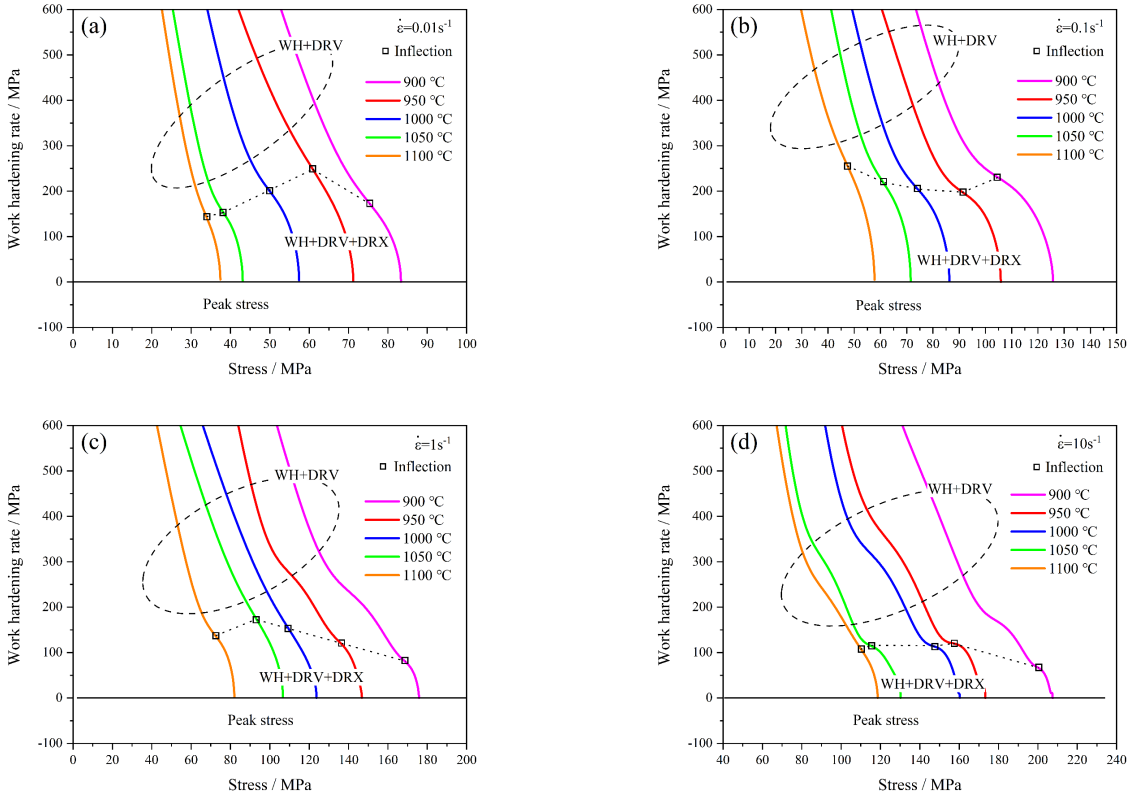

Fig. 8. Work hardening rate curves under evaluated conditions: (a) 0.01 s^{-1}, (b) 0.1 s^{-1}, (c) 1 s^{-1}, and (d) 10 s^{-1}.

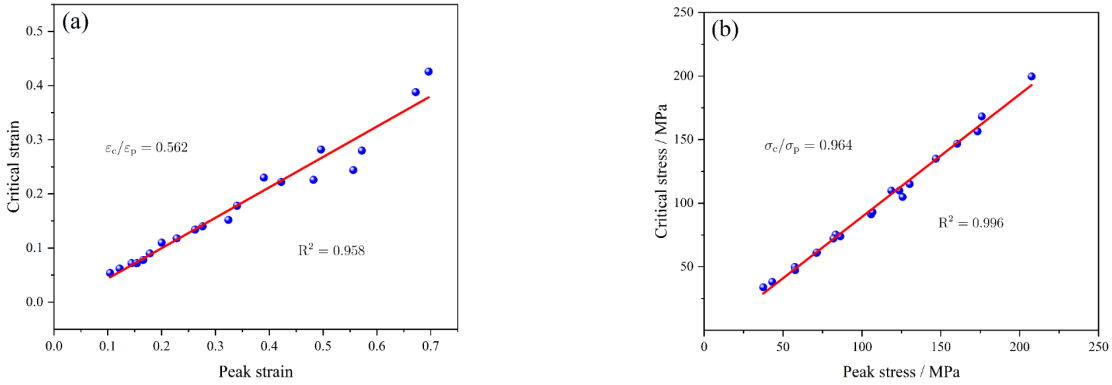

Fig. 9. Peak strain and stress versus (a) critical strain and (b) critical stress.

Notably, DRX is a type of coupling behavior caused by the interplay between stress, temperature, and strain rate.

The thermally activated storage energy generated during the deformation process controls the mechanism of dynamic softening. Therefore, thermally activated storage energy is an important parameter for inducing DRX. Recently, several empirical formulas were proposed to illustrate the relationship between thermally activated stored energy and deformation behavior. The most commonly used formula is the Arrhenius type model, which employs a classical Zener-Hollomon (Z) parameter to represent the coupling effects of the temperature and strain rate [42]:

$$Z = \dot{\varepsilon} exp\left(-\frac{Q}{RT}\right). \tag{1}$$

Moreover, a hyperbolic sine function for different stress levels was proposed by Sellars and Tegart [9, 43, 44]. This function can be used to indicate the relations between thermodynamic parameters:

$$\dot{\varepsilon} = A[\sinh(\alpha\sigma)]^n exp\left(-\frac{Q}{RT}\right) \tag{2}$$

where A, n are materials constants; α is the stress multiplier (MPa^{-1}); Q is the activation energy for deformation (J mol^{-1}); $\dot{\varepsilon}$ is the strain rate (s^{-1}); T is the absolute temperature (K); R is the gas constant (8.314 J/mol^{-1}K^{-1}); and σ is the flow stress (MPa^{-1}). Notably, the peak stress σ_p is generally used to represent σ because it can be more easily and precisely attained from the flow stress curve. σ_p is also an important parameter for industrial processes [45]. To further calculate the values of A, n, and Q, take the logarithm of both sides of Eq. (2); then, the formula can be derived as

$$\ln\left[\sinh\left(\alpha\sigma_p\right)\right] = \frac{\ln\dot{\varepsilon}}{n} + \frac{Q}{nRT} - \frac{\ln A}{n}. \tag{3}$$

The stress exponent n and the activation energy Q can then be calculated using the following equations:

$$\begin{cases} n = \mathrm{R}\dfrac{\partial ln\dot{\varepsilon}}{\partial ln[sinh(\alpha\sigma_p)]}\Big|_T \\ Q = nR\dfrac{\partial ln[sinh(\alpha\sigma_p)]}{\partial(1/T)}\Big|_{\dot{\varepsilon}} \end{cases}. \tag{4}$$

The coefficient of stress multiplier α is an important parameter for calculating n and Q. The stress multiplier α can be obtained using the method in [46]. Then, the variation in n can be obtained by adjusting the value of α over a selected narrow range (0.005-0.02 MPa^{-1}). The value that corresponds to the lowest standard deviation of n at all temperatures is taken to be the most suitable stress multiplier α. In this work, the value of α was calculated to be 0.01 MPa^{-1} for the experimental sample, which is in good agreement with the so-called "traditional value" found in austenitic stainless steels (0.006-0.014) [47]. After that, the linear relationships between $ln[sinh(\alpha\sigma)]$ and $1/T$ and $ln\dot{\varepsilon}$ and $ln[sinh(\alpha\sigma)]$ were fitted, as shown in Fig. 10 (a) and (b). The average values of the slopes for these lines were determined as the numerical values of n and Q. Then, the values of A, n, and Q were calculated as follows: $A = 5.059 \times 10^{12}$, $n = 4.917$, and $Q = 333.968$ kJ/mol. Thus, Eq. (1) and Eq. (2) can be expressed as

$$\dot{\varepsilon} = 5.059 \times 10^{12}[sinh(0.01\sigma)]^{4.917} exp\left(-\frac{333968}{RT}\right) \tag{5}$$

$$Z = \dot{\varepsilon} exp\left(-\frac{333968}{RT}\right) = 5.059 \times 10^{12}[sinh(0.01\sigma)]^{4.917} \tag{6}$$

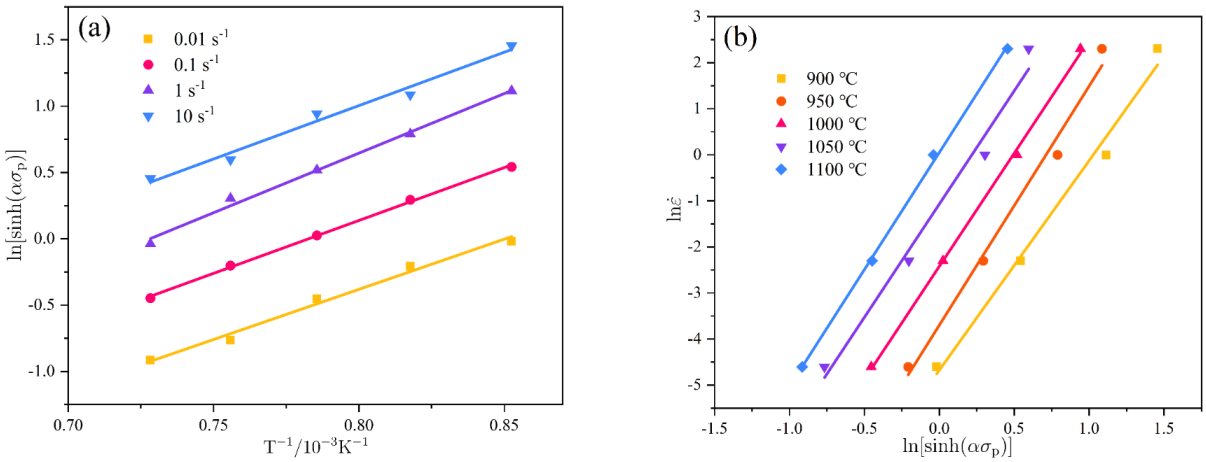

Fig. 10. Linear regression fittings of (a) $ln[sinh(\alpha\sigma_p)] - 1/T$, (b) $ln\dot{\varepsilon} - ln[sinh(\alpha\sigma_p)]$.

Here, there is a linear relationship between the deformation parameters of ε_c, ε_p, σ_c, σ_p and the Z values, as described previously [48, 49]. According to Eq. (1), the Z value corresponding to a given set of experimental conditions can be calculated. The relationship between the deformation parameters of ε_c, ε_p, σ_c, σ_p, and the Z values is shown in Fig. 11. The following equations were obtained:

$$\begin{cases} \varepsilon_c = 0.0005Z^{0.186} \\ \sigma_c = 0.773Z^{0.155} \end{cases} \tag{7}$$

$$\begin{cases} \varepsilon_p = 0.0012Z^{0.179} \\ \sigma_p = 1.0934Z^{0.147} \end{cases}. \tag{8}$$

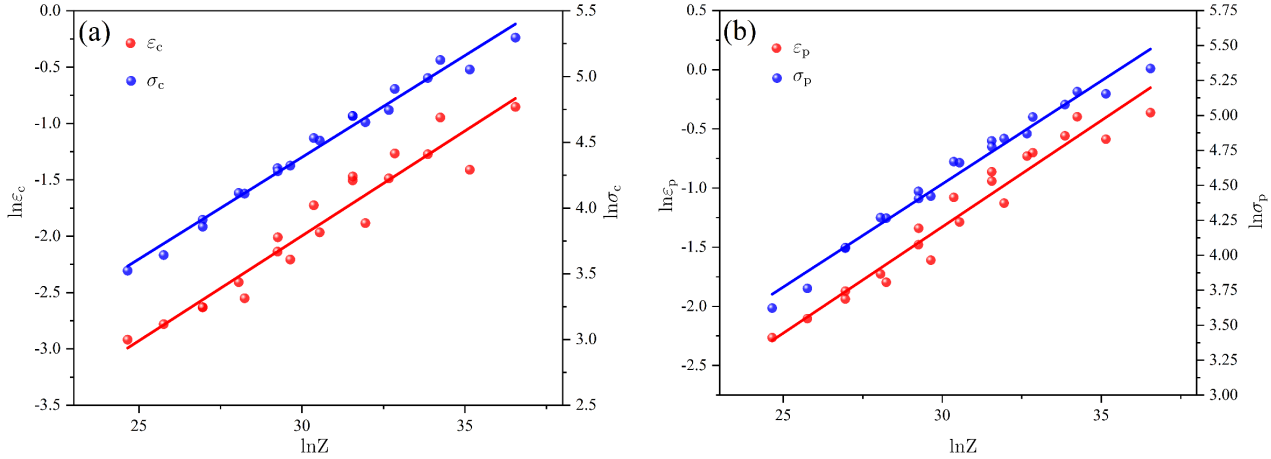

Fig. 11. Relationships between the dimensionless parameter Z and (a) ε_c and σ_c, (b) ε_p and σ_p

3.2. DRX kinetics model

Based on the above analysis, DRX clearly represents a key dynamic softening mechanism during high-temperature deformation. Previously published studies also proposed multiple models for calculating the volume fraction of DRX [50-57]. The results of these will help us better understand the physical meanings of different DRX model parameters. Notably, several studies approximated the peak stress σ_p with the saturated stress σ_{sat} [37, 58, 59]. However, one limitation was found in this case: To further determine the volume fraction of DRX, the onset of DRX was assumed to occur at peak stress. The importance of the dynamic softening mechanism during high-temperature deformation is exemplified by the different occurrences of the critical point (see section 3.1.1). The high precision DRX model depends on the evolution process from the occurrence of DRX to the final evolution process. i.e., the internal softening mechanism of DRX grains. Therefore, it is most appropriate to adopt the difference between DRV saturation stress and steady-state stress as the driving force, considering the relevant characteristics of the dynamic softening process and the limits of DRX onset. The dynamically recovered stress and DRX kinetic model were determined based on the method proposed by Zahiri et al. [60] and Jonas et al. [61], as shown in Eq. (9):

$$X_{\mathrm{DRX}} = \frac{\sigma_{recov} - \sigma}{\sigma_{sat} - \sigma_{ss}} \tag{9}$$

where X_{DRX} is the dynamically recrystallized volume fraction, σ_{recov} is the dynamically recovered stress, σ is the flow stress, σ_{sat} is the saturation stress, and σ_{ss} is the steady-state stress. Here, σ and σ_{ss} can be obtained from the flow stress curves. σ_{recov} is the DRV stress calculated based on the assumption that decreases in the WH rate above the critical stress remain constant. The equations can be generalized in the following form:

$$\theta = d\sigma/d\varepsilon = -s\sigma_{recov} + t \tag{10}$$

The critical stress and saturation stress are two points on a straight line based on substituting the corresponding values into the equation. s and t are expressed in the following equations:

$$s = -\theta_c(\sigma_{sat} - \sigma_c) \tag{11}$$

$$t = -\theta_c\sigma_{sat}(\sigma_{sat} - \sigma_c) \tag{12}$$

where θ_c is the work hardening rate corresponding to the critical stress. Therefore, the stress corresponding to σ_{recov} is estimated as

$$\sigma_{recov} = [(s\sigma_c + t)exp(s\varepsilon - s\varepsilon_c) - t]/s \tag{13}$$

Then, the values of X_{DRX} under different deformation parameters can be obtained from Eq. (9) to establish a prediction model for the DRX volume fraction. The following mathematical model was used to represent variation in the volume fraction of DRX under different deformation conditions [62]:

$$X_{\mathrm{DRX}} = 1 - exp\left(-b\left(\frac{\varepsilon - \varepsilon_c}{\varepsilon_p}\right)^k\right) \tag{14}$$

where k and b are constants under different deformation conditions. Then, Eq. (9) was substituted into Eq. (14). The following equation was subsequently obtained by taking the natural logarithm on both sides:

$$ln[-ln(1 - X_{\mathrm{DRX}})] = ln\, b + k\, ln\left(\frac{\varepsilon - \varepsilon_c}{\varepsilon_p}\right) \tag{15}$$

The experimental value of DRX volume fraction is calculated based on the experimental data (stress-strain curves). Fig. 12 shows a comparison of the experimental and predicted DRX volume fraction under different deformation conditions. The volume fraction of DRX displays an S-type increasing trend that agrees well with the DRX behavior of nonferrous metals presented in previous studies [16]. The predicted values are all consistent with the experimental values of the theoretical model for a 10% to 90% DRX volume fraction. The experimental material underwent a stable DRX process under low strain rate deformation (0.01 s^{-1}), as shown in Fig. 12 (a). Here, the results provide substantial evidence in the flow stress kinetics analysis that at a lower strain rate, the deformed samples had enough time for the grains to nucleate and grow. Finally, the volume fraction of DRX reached 100 %, indicating the complete occurrence of DRX. Briefly, the DRX volume fraction decreased with an increase in the strain rate, which indicates that the material cannot undergo complete recrystallization at a higher strain rate. In this work, at a strain rate of 0.01 s^{-1}, the sample material exhibited significant dynamic softening. Therefore, the average value of k and b were calculated from the lowest strain rates, which were 2.723 and 1.287, respectively. Then, the predicted DRX model was derived and expressed as

$$X_{\mathrm{DRX}} = 1 - exp\left(-1.287\left(\frac{\varepsilon - \varepsilon_c}{\varepsilon_p}\right)^{2.723}\right). \tag{16}$$

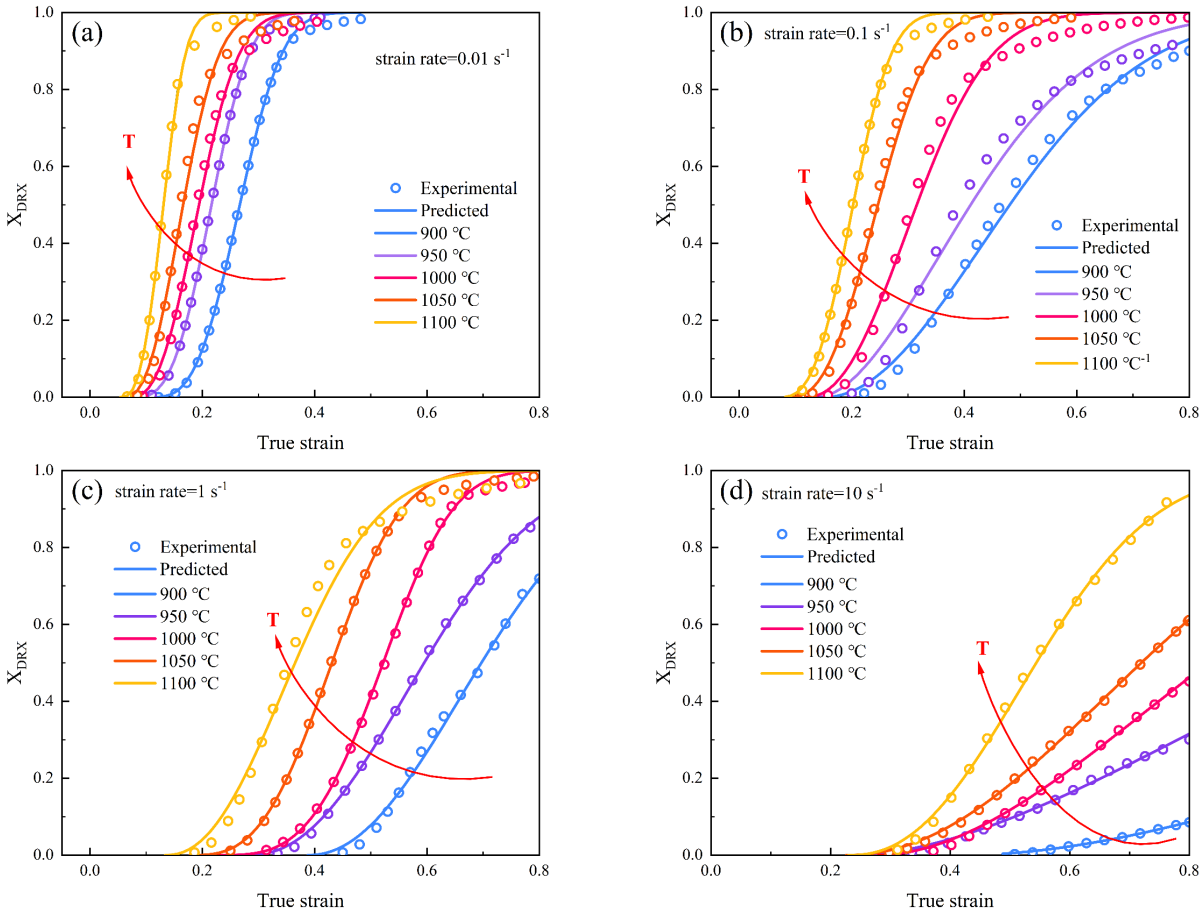

Fig. 12. A comparison of predicted and experimental X_{DRX} values.

To directly validate the predicted model accuracy, the prediction reliability levels of the models were further scientifically evaluated based on the correlation coefficient (R) and root mean square error $(RMSE)$, which was calculated as follows [63]:

$$R = \frac{\sum_{i=1}^{n}(X_i-\bar{X})(Y_i-\bar{Y})}{\sqrt{\sum_{i=1}^{n}(X_i-\bar{X})^2}\sqrt{\sum_{i=1}^{n}(Y_i-\bar{Y})^2}} \tag{17}$$

$$RMSE = \sqrt{\frac{1}{n}\sum_{i=1}^{n}(Y_i - X_i)^2}. \tag{18}$$

where X_i represents the experimental values of X_{DRX}, Y_i represents the predicted values of X_{DRX}, $\bar{X}$ is the average value of the experimental values, and $\bar{Y}$ is the average value of the predicted values. Fig. 13 shows the predicted and experimental X_{DRX} values under all deformation conditions (R and $RMSE$). The R values of the prediction model with strain rates of 0.01, 0.1, 1, and 10 s^{-1} were determined to be 0.99891, 0.99745, 0.99849, and 0.99949, respectively. The $RMSE$ values of the prediction model with strain rates of 0.01, 0.1, 1, and 10 s^{-1} were calculated as 0.01654, 0.02714, 0.02196, and 0.00845, respectively. Considering these results, the developed models are clearly capable of predicting DRX content. These predictions were mainly concentrated around the optimal line, indicating greater prediction accuracy for the DRX volume fraction. Therefore, the developed constitutive equation can be used to describe the DRX behavior of the studied steel under the specified deformation conditions.

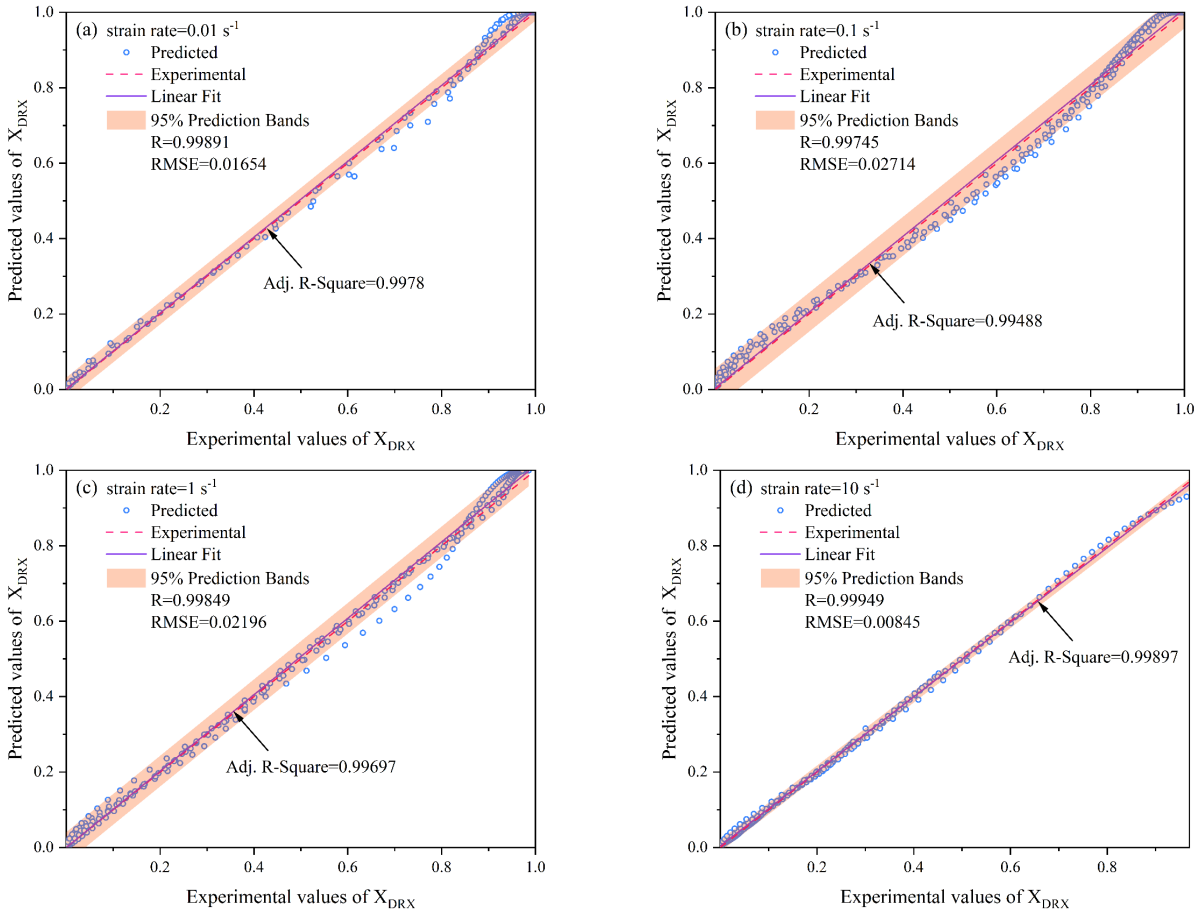

Fig. 13. Comparison of the accuracy of the predicted models.

3.3. Evaluation of the hot processing map for deformation

A hot processing map based on the dynamic materials model (DMM) is capable of reflecting the evolutionary mechanisms of a given material's microstructure and depicting the unstable regions of the thermal deformation process [64-66]. The total energy P input to the system from outside can be divided into two sections of integrals [67, 68]:

$$\begin{cases} P = \sigma\dot{\varepsilon} = G + J \\ G = \int_0^{\dot{\varepsilon}} \sigma d\dot{\varepsilon} \\ J = \int_0^{\sigma} \dot{\varepsilon} d\sigma \end{cases} \tag{19}$$

where G is the energy corresponding to the power generated by increases in temperature, and J is the energy corresponding to the power dissipated by the microstructure's evolution. The relationship between stress and strain assumes that the strain and deformation temperature are constant:

$$\sigma = k\dot{\varepsilon}^m \tag{20}$$

where k is the material constant, and m is the strain rate sensitivity coefficient used to determine the proportion of G and J:

$$m = \frac{\partial J}{\partial G} = \frac{\dot{\varepsilon} \cdot d\sigma}{\sigma \cdot d\dot{\varepsilon}} = \frac{dlg\sigma}{dlg\dot{\varepsilon}}. \tag{21}$$

Combining Eq. (19), (20), and (21), J can be expressed using Eq. (22):

$$J = \int_0^{\sigma} \dot{\varepsilon} d\sigma = \frac{m}{m+1}\sigma\dot{\varepsilon} \tag{22}$$

Momeni et al. [64] indicated that for an ideal linear dissipation process, the value of the strain-rate sensitivity coefficient $m = 1$, resulting in the same values for G and J. Therefore, $J_{max} = \sigma\dot{\varepsilon}/2$. The power dissipation efficiency η is also introduced to evaluate the power dissipation capacity of the material:

$$\eta = \frac{J}{J_{max}} = \frac{\frac{m}{m+1}\sigma\dot{\varepsilon}}{\sigma\dot{\varepsilon}/2} = \frac{2m}{m+1}. \quad (23)$$

The rheological instability factor based on theory of irreversible thermodynamics is given in Eq. (24) [69]:

$$\xi(\dot{\varepsilon}) = \frac{\partial lg\frac{m}{m+1}}{\partial lg\dot{\varepsilon}} + m < 0 \quad (24)$$

where $\xi(\dot{\varepsilon})$ is a dimensionless instability parameter. Rheological instability occurs when the value of $\xi(\dot{\varepsilon}) < 0$. Rheological instability consists of localized flow, adiabatic shear regions, voids and wedge cracks, etc. [70] in the coordinate area where the vertical and horizontal axes represent the deformation temperature and the logarithmic value of the strain rate. The instability map corresponds to $\xi(\dot{\varepsilon}) < 0$, and the power dissipation map corresponds to the value of η, which varies with the deformation temperature and strain rate. The hot processing map represents a spatial superposition of the power dissipation map and instability map [71, 72].

Fig. 14 illustrates the 3D power dissipation efficiency η under different strains. Generally, the DRX region corresponds to relatively high power dissipation, which indicates that the material processing performance has high efficiency in this region [73]. As the figure shows, the peak power dissipation rate η is 57.2%. With a strain of 0.1, the peak region of power dissipation efficiency corresponds to a strain rate of 0.1 s^{-1} and a temperature of 1100 ℃. When the strain increases to 0.5 and 0.7, the power dissipation efficiency decreases with an increase in strain rate and a decrease in deformation temperature. The maximum power dissipation efficiency appears at lower strain rates and higher deformation temperatures. The peak power dissipation efficiency decreases gradually with increasing strain, but the peak region of power dissipation efficiency remains under lower strain-rate conditions. The reason for this phenomenon is the low free energy and critical dislocation density required for DRX at high temperatures with large deformations. The time required to achieve the critical value of DRX under the same strain is different for high and low strain rates. The essence of DRX is the process of the generation, accumulation, and annihilation of dislocations. When the strain rate is low, sufficient time is provided for the accumulation of dislocation energy; hence, DRX can easily occur [21]. Notably, materials deform in the region of high powered dissipation efficiency, which usually affords better workability. However, in some cases, such as wedge cracks and pore instability, higher powered dissipation efficiency is also achieved. Therefore, the optimal processing region cannot be judged only from the value of the power dissipation efficiency η but must also be combined with the instability map.

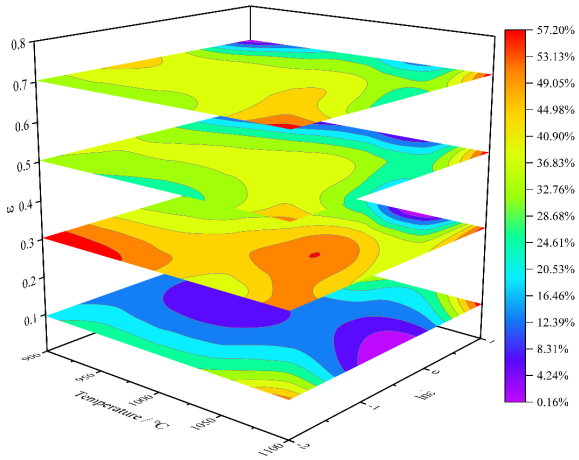

Fig. 14. 3D power dissipation map of experimental steel.

Fig. 15 illustrates the instability map under different strains. Here, the green color represents the stable region, and the purple color represents the instability region. The figure shows that there is a region of instability at a strain range from 0.1 to 0.7. When the strain is 0.1, the instability region corresponds to the low strain rate region. With an increase in strain, the instability region moves primarily toward the high-temperature and high strain rate region. Conversely, the stability region gradually moves toward the high-temperature and low strain rate region.

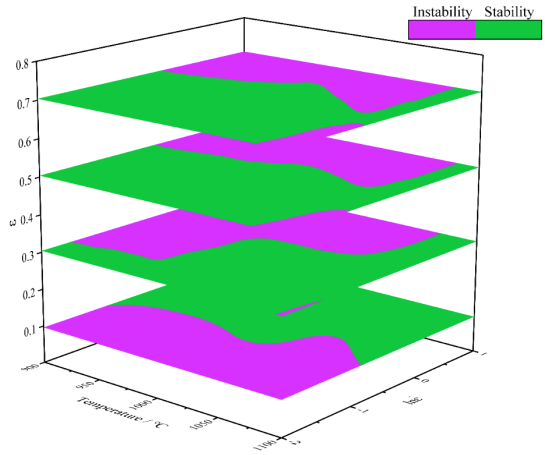

Fig. 15. 3D instability map.

The hot processing map was established by combining a power dissipation map and instability map at a strain of 0.8 under different deformation conditions, as shown in Fig. 16. Previous studies suggested that the power dissipation efficiency and instability regions in hot processing maps represent the microstructural evolution under the current deformation parameters [69, 74, 75]. Notably, some studies showed that when $\eta < 0.3$, dynamic recovery is the main softening mechanism during thermoplastic deformation; when $0.3 \leq \eta \leq 0.6$, dynamic recrystallization is the main softening mechanism; and when $\eta \geq 0.6$, superplastic deformation is the main softening mechanism [76, 77]. Therefore, the processing parameters for the experimental steel were chosen as follows: 900-1050 ℃ and 0.01-1 s^{-1} (i.e., outside the instability region (purple color) and inside the stable region (green color) on the processing map). These findings will also provide guidance for developing an optimal flexible rolling process.

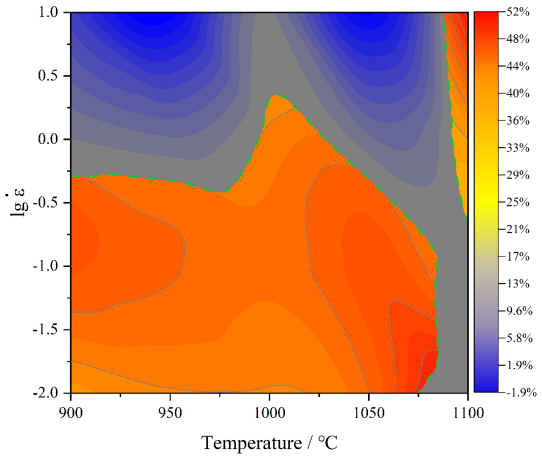

Fig. 16. Processing map with a strain of 0.8 under different deformation parameters.

3.4. Microstructure analysis

The DRX behavior of the specimens was determined by analyzing the deformed microstructures observed through OM. Fig. 17 shows the microstructures of the samples under different deformation temperature and strain rates. When comparing these deformed microstructures to the original microstructure presented in Fig. 3, it can be observed that multiple small grains were formed after deformation, indicating varying degrees of DRX under the specified deformation conditions. Fig. 17 indicates the interference of phase transformations at the grain boundaries due to the inevitable effect of phase transformation during the quenching process of steel materials, especially because the materials used in this paper can more easily experience phase transformations, thereby affecting the clarity of the grain boundaries; however, the grain size can also be judged from the figures. As shown in Fig. 17 (a) and (b), the grain size decreased with an increase in the strain rate, mainly because the grain boundary migration time was sufficient at a lower strain rate. The original crystal grains formed dynamically recrystallized grains through the protrusions, resulting in a high DRX volume fraction. This result is consistent with the observations in the previous studies [17]. The DRX

volume fraction and grain size are significantly reduced with an increase in strain rate. As shown in Fig. 17 (c) and (d), DRX occurred almost completely under this deformation condition, which is related to the deformation temperature. The increase in defamation temperature enhanced the free energy between the new grains and the original grains, which resulted in an increased nucleation rate [78]. In this way, the nucleation rate and growth rate of DRX increased with an increase in deformation temperature, which increased the extent of dynamic softening. These results also provide substantial evidence for the variation in flow stress curves. The critical strain and peak strain gradually decreased with an increase in dynamic softening. When the temperature increased to 1100 °C, the experimental steel underwent full recrystallization and grain growth, mainly due to the high temperature promoting grain boundary migration as the driving force at a constant strain rate. The deformed grains were then gradually swallowed by the DRX grains.

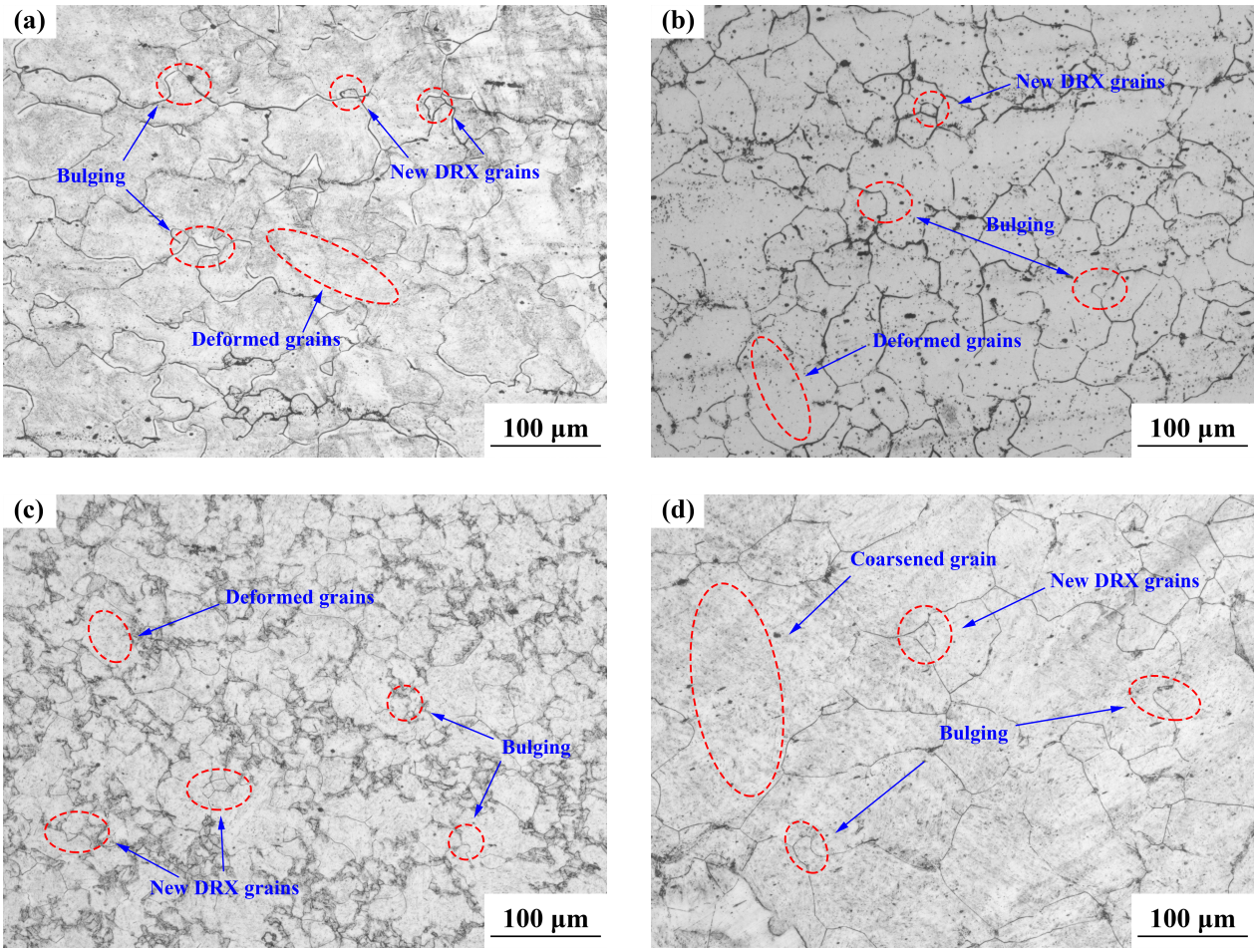

Fig. 17. Microstructures of the specimens under specific deformation conditions: (a) 1000 °C, 0.01s^{-1} (b) 1000 °C, 0.1s^{-1} (c) 900 °C, 0.1s^{-1}, and (d) 1100 °C, 0.1s^{-1}.

Due to the undeniable effects of DRX on the microstructure evolution of materials, changes in the deformation state along the rolling direction of the experimental steel were investigated using OM to determine the grain size. Fig. 18 shows the OM maps at a deformation temperature of 950 °C and strain rate of 1 s^{-1} with different deformation reductions. The corresponding reductions and strains were 0 (0), 18% (0.2), 45% (0.6), and 55% (0.8). Here, the grain size of the samples was greatly affected by the deformation state. The microstructure consisted of austenite equiaxed grains at a reduction of 0% (Fig. 18 (a)). As the deformation state increased, multiple small equiaxed grains were formed after the deformation, indicating the occurrence of DRX and grain gradual refinement. When the deformation was 10% (Fig. 18 (d)), the grain boundary began to bulge and produce serrations.

Therefore, based on the evolution of the grain boundary, the recrystallized grains formed mainly through bulging of the boundaries in the initial grains. This suggests that DRX became less pronounced as the upper roller was raised

and the lower roller was lowered during the flexible rolling process, resulting in a partial DRX state along the thickness transition zone. Notably, partial recrystallization distribution led to a lower hot workability of the material. This phenomenon would be a worthwhile focus for future research, to minimize the degree of recrystallization inhomogeneity.

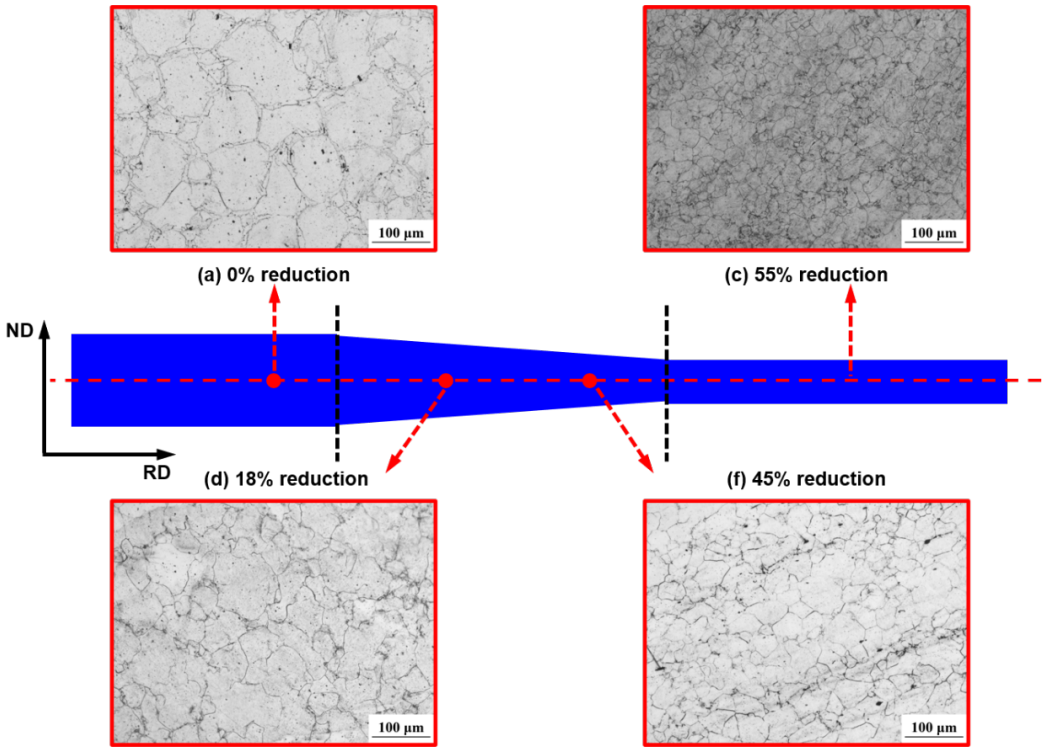

Fig. 18. Microstructure of the flexible rolling process with the specified deformation state along the rolling direction: (a) 0% reduction, (b) 18% reduction, (c) 45% reduction, (d) 55% reduction.

4. Conclusions

Flexible rolling is a significant transformative technology with the potentially to greatly improve future production yields. However, because of the limitations of current rolling technology, it remains difficult to describe the recrystallization behavior of the flexible rolling process in a direct way. In this paper, an equivalent substitution method was designed to describe DRX behavior during the flexible rolling process and thus provide theoretical support for the dynamic softening mechanism. The main conclusions of this study are as follows:

(1) The stress-strain curves for the experimental steel indicate that DRX is the main softening mechanism during deformation at a deformation temperature of 900-1000 °C and a strain rate of 0.01-10 s^{-1}; the peak stress varies with the deformation parameters.

(2) Under high-temperature deformation, work hardening and dynamic softening occurred at different critical stages. The critical strain ε_c and critical stress σ_c for DRX under different deformation parameters were obtained from the work hardening curves. A linear relationship was observed between the critical strain and peak strain and the critical stress and peak stress.

(3) The average activation energy under the specified deformation conditions was about 334 kJ/mol. The Zener-Holomon equation was used to describe the deformation behavior of the material with the coupling effect of strain rate and temperature under high temperature plastic deformation. The correlation between the characteristic points of the flow stress curve and the Z parameter was also obtained.

(4) A new DRX model was proposed by combining the theoretical implications of existing models. The experimental and predicted X_{DRX} values were also compared. All predicted values were found to be consistent with the experimental values, which can be used to describe the DRX of the studied steel.

(5) Hot processing map with strain values of 0.8 were established under different deformation parameters. This

process can be conducted safely at a temperature of 900-1050 ℃ and a strain rate of 0.01-1 s^{-1}. Importantly, the instability region mainly occurs at high strain rates and temperatures, which must be avoided during the flexible rolling process.

(6) A model of DRX microstructure evolution was proposed under the flexible rolling process. The recrystallized grains formed mainly through boundary bulging. DRX decreased as the upper roller was raised and the lower roller was lowered during the flexible rolling process, resulting in a partial DRX state along the thickness transition zone.

CRediT authorship contribution statement:

Caiyi Liu: Conceived, Designed, Performed the experiments, Visualization, Formal analysis, Investigation, Writing-original draft. **Carlo Mapelli:** Investigation, Formal analysis, Writing-review & editing. **Yan Peng:** Conceptualization, Funding acquisition, Supervision, Writing-review & editing. **Silvia Barella:** Writing-review & editing, Investigation, Formal analysis. **Shicheng Liang**: Data curation, Performed the experiments. **Andrea Gruttadauria :** Experiments. **Marco Belfi:** Experiments.

Declaration of competing interest:

The authors declare that they have no known competing financial interests or personal relationships that could have appeared to influence the work reported in this paper.

Acknowledgments:

The present research has been fully supported by Regional Joint Funds of the National Natural Science Foundation of China (Grant No. U20A20289); China Scholarship Council (202008130190); Innovative Research Groups Project of the Natural Science Foundation of Hebei Province, China (Grant No. E2021203011).

References

[1] Z. Li, Y. Chen, S. Wei, F. Xiao, S.H. Siyal, L. Xu, Flow behavior and processing map for hot deformation of W-1.5ZrO2 alloy, Journal of Alloys and Compounds 802 (2019) 118-128.

[2] P.F. Gao, G. Qin, X.X. Wang, Y.X. Li, M. Zhan, G.J. Li, J.S. Li, Dependence of mechanical properties on the microstructural parameters of TA15 titanium alloy with tri-modal microstructure, Materials Science and Engineering A 739 (2019) 203-213.

[3] F. Ren, F. Chen, J. Chen, X. Tang, Hot deformation behavior and processing maps of AISI 420 martensitic stainless steel, Journal of Manufacturing Processes 31 (2018) 640-649.

[4] J. Favre, D. Fabrègue, K. Yamanaka, A. Chiba, Modeling dynamic recrystallization of L-605 cobalt superalloy, Materials Science and Engineering A 653 (2016) 84-92.

[5] M. Zhao, L. Huang, C. Li, J. Li, P. Li, Evaluation of the deformation behaviors and hot workability of a high-strength low-alloy steel, Materials Science and Engineering: A 810 (2021) 141031.

[6] Y. Wu, Z. Liu, X. Qin, C. Wang, L. Zhou, Effect of initial state on hot deformation and dynamic recrystallization of Ni-Fe based alloy GH984G for steam boiler applications, Journal of Alloys and Compounds 795 (2019) 370-384.

[7] J. Liu, X. Wang, J. Liu, Y. Liu, H. Li, C. Wang, Hot deformation and dynamic recrystallization behavior of Cu-3Ti-3Ni-0.5Si alloy, Journal of Alloys and Compounds 782 (2019) 224-234.

[8] L. Li, Y. Wang, H. Li, W. Jiang, T. Wang, C.C. Zhang, F. Wang, H. Garmestani, Effect of the Zener-Hollomon parameter on the dynamic recrystallization kinetics of Mg-Zn-Zr-Yb magnesium alloy, Computational Materials Science 166 (2019) 221-229.

[9] C.M. Sellars, The kinetics of softening processes during hot working of austenite, Czechoslovak Journal of Physics 35(3) (1985) 239-248.

[10] H. Yada, T. Senuma, Resistance to hot deformation of steel, J. JSTP 27(300) (1986).
[11] S.-I. Kim, Y.-C. Yoo, Dynamic recrystallization behavior of AISI 304 stainless steel, Materials Science and Engineering: A 311(1-2) (2001) 108-113.
[12] S.-I. Kim, Y. Lee, D.-L. Lee, Y.-C. Yoo, Modeling of AGS and recrystallized fraction of microalloyed medium carbon steel during hot deformation, Materials Science and Engineering: A 355(1-2) (2003) 384-393.
[13] K. Karhausen, R. Kopp, M.M.D. Souza, Numerical simulation method for designing thermomechanical treatments, illustrated by bar rolling, Scandinavian Journal of Metallurgy 20 (1991) 351-363.
[14] N.D. Ryan, H.J. McQueen, Comparison of dynamic softening in 301, 304, 316 and 317 stainless steels, High temperature technology 8(3) (1990) 185-200.
[15] S. Serajzadeh, A. Karimi Taheri, Prediction of flow stress at hot working condition, Mechanics Research Communications 30(1) (2003) 87-93.
[16] J. Liu, Z. Cui, L. Ruan, A new kinetics model of dynamic recrystallization for magnesium alloy AZ31B, Materials Science and Engineering A 529(1) (2011) 300-310.
[17] C. Li, L. Huang, M. Zhao, X. Zhang, J. Li, P. Li, Influence of hot deformation on dynamic recrystallization behavior of 300M steel: Rules and modeling, Materials Science and Engineering: A 797 (2020) 139925.
[18] H. Ji, Z. Cai, W. Pei, X. Huang, Y. Lu, DRX behavior and microstructure evolution of 33Cr23Ni8Mn3N: Experiment and finite element simulation, Journal of Materials Research and Technology 9(3) (2020) 4340-4355.
[19] B. Shen, L. Deng, X. Wang, A new dynamic recrystallisation model of an extruded Al-Cu-Li alloy during high-temperature deformation, Materials Science and Engineering A 625 (2015) 288-295.
[20] C. Zhang, C. Wang, R. Guo, G. Zhao, L. Chen, W. Sun, X. Wang, Investigation of dynamic recrystallization and modeling of microstructure evolution of an Al-Mg-Si aluminum alloy during high-temperature deformation, Journal of Alloys and Compounds 773 (2019) 59-70.
[21] M. Zhao, L. Huang, C. Li, J. Li, P. Li, Evaluation of the deformation behaviors and hot workability of a high-strength low-alloy steel, Materials Science and Engineering A 810 (2021).
[22] Y.-Q. Jiang, Y.C. Lin, G.-Q. Wang, G.-D. Pang, M.-S. Chen, Z.-C. Huang, Microstructure evolution and a unified constitutive model for a Ti-55511 alloy deformed in β region, Journal of Alloys and Compounds 870 (2021) 159534.
[23] X. Wang, K. Chandrashekhara, S.N. Lekakh, D.C. Van Aken, R.J. O'Malley, Modeling and Simulation of Dynamic Recrystallization Behavior in Alloyed Steel 15V38 during Hot Rolling, steel research international 90(4) (2019) 1700565.
[24] M. Zhao, L. Huang, R. Zeng, H. Su, D. Wen, J. Li, In-situ observations and modeling of metadynamic recrystallization in 300M steel, Materials Characterization 159 (2020).
[25] J.S. Nagra, A. Brahme, J. Lévesque, R. Mishra, R.A. Lebensohn, K. Inal, A new micromechanics based full field numerical framework to simulate the effects of dynamic recrystallization on the formability of HCP metals, International Journal of Plasticity 125 (2020) 210-234.
[26] Q. Luo, Y. Guo, B. Liu, Y. Feng, J. Zhang, Q. Li, K. Chou, Thermodynamics and kinetics of phase transformation in rare earth-magnesium alloys: A critical review, Journal of Materials Science and Technology 44 (2020) 171-190.
[27] P. Gao, M. Fu, M. Zhan, Z. Lei, Y. Li, Deformation behavior and microstructure evolution of titanium alloys with lamellar microstructure in hot working process: A review, Journal of Materials Science and Technology 39 (2020) 56-73.
[28] R. Zeng, L. Huang, J. Li, H. Li, H. Zhu, X. Zhang, Quantification of multiple softening processes occurring during multi-stage thermoforming of high-strength steel, International Journal of Plasticity 120 (2019) 64-87.
[29] M.S. Chen, W.Q. Yuan, H.B. Li, Z.H. Zou, New insights on the relationship between flow stress softening and dynamic recrystallization behavior of magnesium alloy AZ31B, Materials Characterization 147 (2019) 173-183.
[30] L. Chen, W. Sun, J. Lin, G. Zhao, G. Wang, Modelling of constitutive relationship, dynamic recrystallization and grain size of 40Cr steel during hot deformation process, Results in Physics 12 (2019) 784-792.
[31] Z.M. Cai, H.C. Ji, W.C. Pei, X.M. Huang, W.D. Li, Y.M. Li, Constitutive model of 3Cr23Ni8Mn3N heat-resistant steel based on back propagation (BP) neural network(NN), Metalurgija 58(3-4) (2019) 191-195.

[32] Z. Cai, H. Ji, W. Pei, X. Tang, X. Huang, J. Liu, Hot workability, constitutive model and processing map of 3Cr23Ni8Mn3N heat resistant steel, Vacuum 165 (2019) 324-336.
[33] M. Annasamy, N. Haghdadi, A. Taylor, P. Hodgson, D. Fabijanic, Dynamic recrystallization behaviour of AlxCoCrFeNi high entropy alloys during high-temperature plane strain compression, Materials Science and Engineering A 745 (2019) 90-106.
[34] C. Ghosh, C. Aranas Jr, J.J. Jonas, Dynamic transformation of deformed austenite at temperatures above the Ae3, Progress in Materials Science 82 (2016) 151-233.
[35] S. Solhjoo, Determination of flow stress and the critical strain for the onset of dynamic recrystallization using a hyperbolic tangent function, Materials and Design 54 (2014) 390-393.
[36] J. Zou, J. Chen, H. Yan, W. Xia, B. Su, Y. Lei, Q. Wu, Effects of Sn addition on dynamic recrystallization of Mg-5Zn-1Mn alloy during high strain rate deformation, Materials Science and Engineering A 735 (2018) 49-60.
[37] Y. Han, S. Yan, B. Yin, H. Li, X. Ran, Effects of temperature and strain rate on the dynamic recrystallization of a medium-high-carbon high-silicon bainitic steel during hot deformation, Vacuum 148 (2018) 78-87.
[38] P. Zhang, C. Yi, G. Chen, H. Qin, C. Wang, Constitutive model based on dynamic recrystallization behavior during thermal deformation of a nickel-based superalloy, Metals 6(7) (2016).
[39] H. Mirzadeh, A. Najafizadeh, Prediction of the critical conditions for initiation of dynamic recrystallization, Materials & Design 31(3) (2010) 1174-1179.
[40] E.I. Poliak, J.J. Jonas, A one-parameter approach to determining the critical conditions for the initiation of dynamic recrystallization, Acta Materialia 44(1) (1996) 127-136.
[41] C. Zhang, L. Zhang, Q. Xu, Y. Xia, W. Shen, The kinetics and cellular automaton modeling of dynamic recrystallization behavior of a medium carbon Cr-Ni-Mo alloyed steel in hot working process, Materials Science and Engineering A 678 (2016) 33-43.
[42] Y. Wang, J. Wang, J. Dong, A. Li, Z. Li, G. Xie, L. Lou, Hot deformation characteristics and hot working window of as-cast large-tonnage GH3535 superalloy ingot, Journal of Materials Science and Technology 34(12) (2018) 2439-2446.
[43] C.M. Sellars, J.A. Whiteman, Recrystallization and grain growth'in hot rolling, Metal Science 13(3-4) (1979) 187-194.
[44] C.M. Sellars, W.J. McTegart, On the mechanism of hot deformation, Acta Metallurgica 14(9) (1966) 1136-1138.
[45] H. Mirzadeh, A. Najafizadeh, M. Moazeny, Flow curve analysis of 17-4 PH stainless steel under hot compression test, Metallurgical and Materials Transactions A 40(12) (2009) 2950.
[46] K.A. Babu, S. Mandal, C.N. Athreya, B. Shakthipriya, V.S. Sarma, Hot deformation characteristics and processing map of a phosphorous modified super austenitic stainless steel, Materials & Design, 115 (2017) 262-275.
[47] H.J. McQueen, N.D. Ryan, Constitutive analysis in hot working, Materials Science and Engineering: A, 322 (2002) 43-63.
[48] X. Wang, C. Huang, B. Zou, H. Liu, H. Zhu, J. Wang, Dynamic behavior and a modified Johnson-Cook constitutive model of Inconel 718 at high strain rate and elevated temperature, Materials Science and Engineering: A 580 (2013) 385-390.
[49] Y. Wang, W. Shao, L. Zhen, B. Zhang, Hot deformation behavior of delta-processed superalloy 718, Materials Science and Engineering: A 528(7-8) (2011) 3218-3227.
[50] C. Li, Y. Tan, F. Zhao, Finite element simulation and process optimization of microstructure evolution in the formation of Inconel 718 alloy bolts, Materials Research Express 6(2) (2019).
[51] L. Lan, W. Zhou, R.D.K. Misra, Effect of hot deformation parameters on flow stress and microstructure in a low carbon microalloyed steel, Materials Science and Engineering A 756 (2019) 18-26.
[52] L. Wang, G. Fang, L. Qian, Modeling of dynamic recrystallization of magnesium alloy using cellular automata considering initial topology of grains, Materials Science and Engineering A 711 (2018) 268-283.
[53] H. Vafaeenezhad, S.H. Seyedein, M.R. Aboutalebi, A.R. Eivani, An investigation of workability and flow instability of Sn-5Sb lead free solder alloy during hot deformation, Materials Science and Engineering A 718 (2018) 87-95.

[54] C. Li, Y. Liu, Y. Tan, F. Zhao, Hot deformation behavior and constitutive modeling of H13-mod steel, Metals 8(10) (2018).
[55] N.R. Jaladurgam, A.K. Kanjarla, Hot deformation characteristics and microstructure evolution of Hastelloy C-276, Materials Science and Engineering A 712 (2018) 240-254.
[56] A. Hadadzadeh, F. Mokdad, M.A. Wells, D.L. Chen, Modeling dynamic recrystallization during hot deformation of a cast-homogenized Mg-Zn-Zr alloy, Materials Science and Engineering A 720 (2018) 180-188.
[57] G. Zhou, Z. Li, D. Li, Y. Peng, H.S. Zurob, P. Wu, A polycrystal plasticity based discontinuous dynamic recrystallization simulation method and its application to copper, International Journal of Plasticity 91 (2017) 48-76.
[58] A.I. Fernández, P. Uranga, B. López, J.M. Rodriguez-Ibabe, Dynamic recrystallization behavior covering a wide austenite grain size range in Nb and Nb-Ti microalloyed steels, Materials Science and Engineering: A 361(1) (2003) 367-376.
[59] M.H. Wang, Y.F. Li, W.H. Wang, J. Zhou, A. Chiba, Quantitative Analysis of Work Hardening and Dynamic Softening Behavior of low carbon alloy Steel Based on the Flow Stress, Materials and Design 45 (2013) 384-392.
[60] S.H. Zahiri, C.H.J. Davies, P.D. Hodgson, A mechanical approach to quantify dynamic recrystallization in polycrystalline metals, Scripta Materialia 52(4) (2005) 299-304.
[61] J.J. Jonas, X. Quelennec, L. Jiang, É. Martin, The Avrami kinetics of dynamic recrystallization, Acta materialia 57(9) (2009) 2748-2756.
[62] A. Laasraoui, J. Jonas, Recrystallization of austenite after deformation at high temperatures and strain rates-analysis and modeling, Metallurgical Transactions A 22(1) (1991) 151-160.
[63] A. Marandi, A. Zarei-Hanzaki, N. Haghdadi, M. Eskandari, The prediction of hot deformation behavior in Fe-21Mn-2.5 Si-1.5 Al transformation-twinning induced plasticity steel, Materials Science and Engineering: A 554 (2012) 72-78.
[64] A. Momeni, K. Dehghani, Characterization of hot deformation behavior of 410 martensitic stainless steel using constitutive equations and processing maps, Materials Science and Engineering A 527(21-22) (2010) 5467-5473.
[65] H.C. Ji, H.L. Duan, Y.G. Li, W.D. Li, X.M. Huang, W.C. Pei, Y.H. Lu, Optimization the working parameters of as-forged 42CrMo steel by constitutive equation-dynamic recrystallization equation and processing maps, J. Mater. Res. Technol. 9(4) (2020) 7210-7224.
[66] X. Ding, F. Zhao, Y. Shuang, L. Ma, Z. Chu, C. Zhao, Characterization of hot deformation behavior of as-extruded AZ31 alloy through kinetic analysis and processing maps, Journal of Materials Processing Technology 276 (2020).
[67] Y.V.R.K. Prasad, T. Seshacharyulu, Modelling of hot deformation for microstructural control, International Materials Reviews 43(6) (1998) 243-258.
[68] Y.V.R.K. Prasad, H.L. Gegel, S.M. Doraivelu, J.C. Malas, J.T. Morgan, K.A. Lark, D.R. Barker, Modeling of dynamic material behavior in hot deformation: Forging of Ti-6242, Metallurgical Transactions A 15(10) (1984) 1883-1892.
[69] Y.V.R.K. Prasad, T. Seshacharyulu, Processing maps for hot working of titanium alloys, Materials Science and Engineering A 243(1-2) (1998) 82-88.
[70] Y. Cao, H. Di, J. Zhang, T. Ma, J. Zhang, Research on hot deformation behavior and hot workability of alloy 800H, Jinshu Xuebao/Acta Metallurgica Sinica 49(7) (2013) 811-821.
[71] Y. Sun, Z. Wan, L. Hu, J. Ren, Characterization of hot processing parameters of powder metallurgy TiAl-based alloy based on the activation energy map and processing map, Materials & Design 86 (2015) 922-932.
[72] R. Ravi, Y.V.R.K. Prasad, V.V.S. Sarma, Development of expert systems for the design of a hot-forging process based on material workability, Journal of Materials Engineering and Performance 12(6) (2003) 646-652.
[73] X. Zhou, K. Wang, S. Lu, X. Li, R. Feng, M. Zhong, Flow behavior and 3D processing map for hot deformation of Ti-2.7Cu alloy, Journal of Materials Research and Technology 9(3) (2020) 2652-2661.
[74] E. Pu, W. Zheng, Z. Song, H. Feng, H. Dong, Hot deformation characterization of nickel-based superalloy UNS10276 through processing map and microstructural studies, Journal of Alloys and Compounds 694 (2017) 617-631.
[75] F. Zhang, J.L. Sun, J. Shen, X.D. Yan, J. Chen, Flow behavior and processing maps of 2099 alloy, Materials Science

and Engineering A 613 (2014) 141-147.
[76] K. Wang, S. Lu, M.W. Fu, X. Li, X. Dong, Optimization of β/near-β forging process parameters of Ti-6.5Al-3.5Mo-1.5Zr-0.3Si by using processing maps, Materials Characterization 60(6) (2009) 492-498.
[77] X. Zhang, Q. Yan, C. Yang, T. Wang, C. Ge, Microstructure, mechanical properties and bonding characteristic of deformed tungsten, International Journal of Refractory Metals and Hard Materials 43 (2014) 302-308.
[78] Y.B. Tan, Y.H. Ma, F. Zhao, Hot deformation behavior and constitutive modeling of fine grained Inconel 718 superalloy, Journal of Alloys and Compounds 741 (2018) 85-96.